Growth and Structural Characterization of Doped Polymorphic Crystalline MgPc as an Organic Semiconductor

Leon Hamui [1,*] , **María Elena Sánchez-Vergara** [1] , **Rocio Sánchez-Ruiz** [1,2] ,
Cecilio Álvarez-Toledano [3] , **Jose Luis Reyes-Rodriguez** [2] and **Arturo Ponce** [2]

[1] Facultad de Ingeniería, Universidad Anáhuac México, Avenida Universidad Anáhuac 46,
    Col. Lomas Anáhuac, Huixquilucan 52786, Estado de México, Mexico;
    elena.sanchez@anahuac.mx (M.E.S.-V.); chiosanchezr@gmail.com (R.S.-R.)
[2] Department of Physics & Astronomy, The University of Texas at San Antonio, One UTSA circle, San Antonio,
    TX 78249, USA; jluisreyesr21@gmail.com (J.L.R.-R.); arturo.ponce@utsa.edu (A.P.)
[3] Instituto de Química, Universidad Nacional Autónoma de México, Circuito exterior s/n,
    Ciudad Universitaria, Coyoacán, México D.F. 04510, Mexico; cecilio@unam.mx
* Correspondence: leon.hamui@anahuac.mx; Tel.: +52-55-5627-0210

check for updates

Abstract: The doping and crystallization of the molecular semiconductor formed from the magnesium phthalocyanine (MgPc) and 1-(4-Methoxyphenyl)-2,2,6,6-tetramethyl-5-phenylhepta-3,4-dienedioic (MTPDA) acid was carried out in this work. The crystals obtained were characterized by using transmission electronic microscopy (TEM), Raman spectroscopy, and X-Ray diffraction (XRD), to later evaluate their optical behavior. Raman, IR, and UV–Vis results indicate that the MgPc has been doped with the MTPDA. A uniform material layer with particles is observed as a result of a two-stage process, nucleation and growth. The polycrystalline films are constituted by a mixture of α and β phases with crystalline sizes of ~7 nm, 14 nm, and 20 nm average sizes. The films exhibit a preferred orientation along the [001]. The MTPDA doping does not have an important effect on the molecule planar distances indicating that the MTPDA molecule is among the equivalent MgPc plane direction. A transparent region with a minimum at 483 nm is observed, also a *B*-band at 337 nm and a Q-band transition with a high-energy peak around 639 nm, and a low energy peak around 691 nm.

Keywords: organic semiconductors; metallophthalocyanine; thin films; Raman spectroscopy; structural analysis

1. Introduction

New alternatives have been developed for conventional electronic devices made up mainly by inorganic semiconductors, i.e., those devices fabricated based on silicon and germanium technologies. The need of new materials comes from the high costs that represent the production, either bottom-up and top-down processing, of standard electronic devices in nanotechnology due to the complexity of conventional fabrication methods. In this way, several methodologies have been proposed using organic routes, specifically for organic semiconductor materials, which allows not only the fabrication of electronic devices at low cost, but also the possibility of tune the electrical and optical properties by engineering mainly π-conjugated systems. There is a wide variety of organic semiconductors, so their classification can be based on size, applications, rheological properties, etc. Based on compounds families, organic semiconductors can be classified into oligoacenes, small molecules, polymers, discotic systems, charge transfer complexes, fullerenes, and graphenes [1–3]. Metallophthalocyanines (MPcs) are within the group of discotic systems [1–3] formed by a functionalized aromatic nucleus. The MPcs have

shown great chemical diversity due to their central cavity, which can be replaced with approximately 70 different metallic ions and other organic ligands [4]. MPcs show π-conjugated macrocycles [5], long and strong wavelength absorption values, and high efficiency when generating reactive oxygen species [6]. Their peculiar Van der Waals interactions [7] and their feasible chemical modification, makes them suitable as good candidates for applications in microelectronics and nanophotonics [8], for instance as in the photocopier industry [4]. In thin films form, the MPcs have been used for the development of photosensitizers [6], organic light emitting diodes (OLEDs), organic field-effect transistors (OFET), dye-sensitized solar cells [9,10] and photoinitiators [11]. MPcs can be deposited as thin films by physical or chemical methods, depending on the desired thickness. For example, vacuum thermal evaporation is a common method to obtain films below 1 μm thick and without degradation, due to the thermal stability of the MPcs molecules [12,13]. On the other hand, crystallization of MPcs compounds is important to tune the physical properties and the correlation with the crystalline structures for device applications. The MPcs molecules exhibit a tendency to order in crystalline phases, due to the aromatic rings stacking. The attractive forces between aromatic rings are mainly π-π interactions and hydrogen bonds. These interactions facilitate the formation of different crystalline phases, which are highly dependent on the substituents in the macrocycle and the molecules orientation and spacing [9,14]. In addition, the deposit conditions and their thermal annealing post-treatments determine the molecular orientations and the crystallinity of the films [14–16]. Crystallization in MPcs may be present in two different angle arrangements between the axis and the stacking direction: the α-crystals and β-crystals. The formed angle between the symmetry axis and the stacking direction for α-crystals is of 26.5° and for β-crystals is of 45.8° [17,18]. Each of the crystalline arrangements has its characteristic opto-electronic behavior, since the orientation of molecules modify the π transitions and, the Q and Soret (B) bands [19]. It has been identified five transition bands for the MPcs, labeled as Q, B, N, L, and C bands [20]. On electronic devices applications, particularly thin films deposited solid-state devices, the absorption spectrum responds to different broad bands assigned to two π-π* transitions systems: a B band in the blue region and a Q band in the red region [19]. Characterization of MPcs through Raman spectroscopy allows the identification of the bands, assigned in an analogous manner by two π-π* transitions, to a B or Soret band in the blue region and a Q band with the associated vibration bands in the red region [19,21].

　　　In the present work, the aim is to develop an organic semiconductor capable of being used in optoelectronic devices. Previous works have demonstrated that incorporating doping on MPc could lead to interesting applications like membrane base optoelectronic devices [10]. However, a deeper study should be done in order to understand the material's capability to work as semiconductor and to understand the effect of the doping on the structural and optoelectronic properties. The last derived from the carrier transport mechanisms during conduction, and photogenerated carrier during light absorption, which would lead to a best selection of the doping material properties for a specific application. Raman spectroscopy was performed on magnesium doped MPc (MgPc) with 1-(4-Methoxyphenyl)-2,2,6,6-tetramethyl-5-phenylhepta-3,4-dienedioic acid and crystallized by diffusion, the results obtained were complemented by IR spectroscopy. Transmission Electron Microscopy (TEM) was carried out for the doped MgPc crystals to determine the crystalline structure analyzed by the electron diffraction patterns of the molecules. Structures of the mentioned molecules are shown in Figure 1. High-resolution transmission electron microscopy (HRTEM) imaging provided information about crystalline lattices of the samples. Later, the thin films were measured by UV–Vis spectroscopy to complement the information about the Q and B bands. To generate a probable improvement on the optoelectronic properties of the MgPc, the 1-(4-Methoxyphenyl)-2,2,6,6-tetramethyl-5-phenylhepta-3,4-dienedioic acid was used dope the compound within the thin films. MgPc is used for its ability to act as a donor species and an electronic acceptor [6,7,11,20,22], while dienedioic acid is chosen because is a compound capable of receiving electrons [22]. The dienedioic acid has two contiguous C=C bonds and also aromatic groups, which have an alternation between double and single bonds, that favors electronic delocalization and the

formation of conduction channels [23,24]. Additionally, the dienedioic acid can act as a nucleophile or an electrophile [23,25,26], which allows its interaction with the central metal ion, and with the macrocycle of the MgPc. The latter favors the charges transport through the available "p" orbitals in the magnesium ion and also due to the electronic delocalization generated in the flat MgPc macrocycle. All of this indicates that the dienedioic acid has an interesting potential for MgPc Doping. To deepen and clarify the above, doped MgPc optical activation energy was determined by UV–Vis spectroscopy and the electrical behavior with increasing temperature, is also determinated.
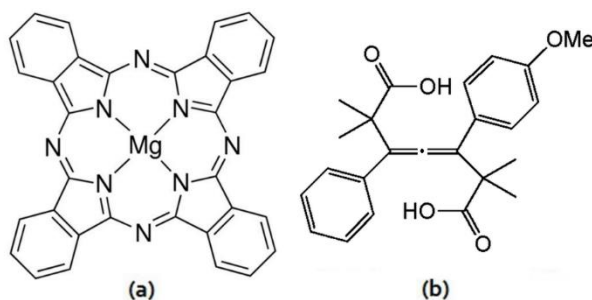
Figure 1. Structure of (**a**) MgPc and (**b**) 1-(4-Methoxyphenyl)-2,2,6,6-tetramethyl-5-phenylhepta-3,4-dienedioic acid.

2. Materials and Methods

Magnesium phthalocyanine (MgPc) ($C_{32}H_{16}N_8Mg$, Dye content: 90%), shown in Figure 1a, was purchased from Sigma-Aldrich (Saint Louis, MO, USA) without any further purification. The magnesium phthalocyanine (MgPc) was doped with 1-(4-Methoxyphenyl)-2,2,6,6-tetramethyl-5-phenylhepta-3,4-dienedioic acid (MTPDA) purchased from Sigma-Aldrich (Saint Louis, MO, USA) without any further purification. The doping process was previously reported by some authors of the present study [17,22]. MgPc-MTPDA was dissolved in a methanol/*n*-hexane mixture and crystals were obtained through a slow evaporation of solvents at room temperature. Raman characterization was carried out on the MgPc-MTPDA crystallized samples using a Raman spectrometer (Horiba, Ltd., Kyoto, Japan) with two laser wavelengths; 532 nm (green laser) and 785 nm (red laser), to determine the displacements of the molecular bond vibrations. Each sample was analyzed with both laser wavelengths and averaged at least with 3 spots in different regions of sample. The resulting spectra show information in a 400–1800 cm^{-1} range about the vibrational states of the material, which allows the analysis of the bonds between MgPc and its dopant. The laser power was adjusted and did not cause any visible alteration to the sample. The MgPc-MTPDA crystals were analyzed on a field emission gun JEOL 2010F transmission electron microscope (JEOL, Ltd., Akishima, Tokyo, Japan) coupled with a highly sensitive CMOS camera, which allow to collect images under low electron dosage to prevent damage in the organic compounds. In order to index the electron diffraction patterns, simulations have been performed using the java version of the electron microscopy simulation software package (JEMS) [27]. FT-IR (Fourier transform infrared) spectroscopy was carried out on the MgPc-MTPDA using a Nicolet iS5-FT spectrometer (Thermo Fisher Scientific Inc., Waltham, Massachusetts, USA) to determine the functional groups present in the molecule.

MgPc-MTPDA films were fabricated through high vacuum evaporation process (Intercovamex, Morelos, México) and a subsequent deposition into (100) single-crystalline silicon (c-Si) 200 Ω-cm wafers and quartz. The heating source was a tungsten boat with a slowly increasing of temperature to 498 K. The selected pressure in the vacuum chamber was 1×10^{-5} torr before the film deposition and the evaporation rate was 0.4 Å/s. A film thickness of 2.3 nm was obtained from a quartz crystal monitor during deposition. The MgPc-MTPDA thin films deposited on quartz substrate were analyzed in SEM (scanning electron microscopy) using a Zeiss EVO MA 10 scanning electron microscope (Carl Zeiss AG, Oberkochen, Germany) operated at 3 kV voltage with a 13.5 mm focal distance. Samples of MgPc-MTPDA films on silicon substrate were analyzed by X-ray diffraction by the θ-2θ technique,

using a Bragg-Brentano geometry on a Bruker D8 Advance diffractometer (Bruker Corporation, Billerica, MA, USA) with a CuK-α (λ = 0.15405 nm) radiation source. UV–Vis spectrometry allowed the measurement of the optical transmittance and absorption of thin film MgPc-MTPDA samples on quartz substrate in the 1100–200 nm range using an UV–Vis spectrophotometer (Thermo Fisher Scientific Inc., Waltham, MA, USA). Finally, Silver contacts were evaporated for electrical measurements. The electrical I–V characteristics were measured in the 0–10 V range, with a channel width and length of ~19 and 1 mm respectively, using a sensing station with a temperature-controlled circuit from Next Robotix (Comercializadora K Mox, S.A. de C.V., Mexico City, Mexico) and an auto-ranging Keithley 4200-SCS-PK1 pico-ammeter (Tektronix Inc., Beaverton, OR, USA).

3. Results

The Crystallized MgPc-MTPDA Raman spectrum is shown on Figure 2 where the maximum peak positions were labeled for analysis. Previous works have calculated the Raman scattering for the MgPc, which gives evidence of the characteristic vibrational Raman shift of these MPcs [28–33]. The Raman bands correspond to deformations and stretching bond vibrations, and characteristic Mg-N bonds vibrations. The most intense peaks were found to be approximately in the 1200–1600 cm^{-1} interval. First, it is reported that the ~1500–1550 cm^{-1} MPc Raman peak shifts depending on the central atom [29]. The aromatic vibration mode shown on Figure 2 is observed at 1501 cm^{-1}, which is related to the A1g symmetry. Second, MPc may present different polymorphic forms as α, β mainly. These forms can be distinguished by main macrocycle Raman shift on the stretching vibration [28–33]. The peaks at 588 and 1141 cm^{-1} present a shift to lower wavelengths indicating the presence of an α-phase in the MgPc. Although, the presence of the 773 cm^{-1}, 1199 cm^{-1} peaks and a shoulder at 1307 cm^{-1} and their shift to higher wavelengths indicate the presence of a β-phase [28]. Therefore, the MgPc is constituted by both, α and β, polymorphic phases. Furthermore, the most intense Raman scattering mode is at 1335 cm^{-1} with symmetry A1g and a shoulder at ~1310 cm^{-1} with symmetry B1g. The second most intense mode of the MgPc is at 1435 cm^{-1} with symmetry B1g. Moreover, it can be observed vibration mode at 1573 cm^{-1} with symmetry B1g for the MgPc and aromatic groups due to their enhanced change of dipole moments. Further analysis should be done to understand the peaks shown on Figure 2 for the crystallized MgPc-MTPDA, which indicate different features. The most intense peak (1335 cm^{-1}) can be attributed to the MgPc C-N stretching mode and C-H in plane H bending mode. The 682 cm^{-1} band is related to the Mg central atom of the crystallized phthalocyanine for the Mg-N vibration mode. The 773 cm^{-1} band is related to the antisymmetric stretching of the MgPc C-N-C bonds. The ~882 cm^{-1} band is related to the MTPDA C-C-O stretching and C-C skeltan vibrations. The 985 cm^{-1} band is related to the MgPc and MTPDA C-H in plane bending. The 1099 cm^{-1} band is related to the C=C=C stretching in dienedioic acid MTPDA, MTPDA stretching C-C-O characteristic band and MTPDA C-H in plane H bending. The 1141 cm^{-1} band is related to the MgPc α phase and MTPDA C-H in plane bending of the aromatic rings. The 1199 cm^{-1} band is related to the aromatic C-H in plane H bending of the MgPc β-phase. The 1435 cm^{-1} band is related to the MTPDA C-O-H deformation mode, MgPc N=C=N symmetric stretching mode, MTPDA CH$_3$ antisymmetric stretching mode, aromatic ring stretching and aromatic ring bending-stretching combined mode. The 1501 cm^{-1} band is related to aromatic ring bending-stretching combined mode and aromatic ring stretching. The 1573 cm^{-1} band is associated to aromatic ring bending-stretching combined mode and aromatic ring stretching. Lastly, the 1689 cm^{-1} band is associated to the MTPDA C=C stretching mode, MTPDA C=O symmetric and antisymmetric stretching modes and the MTPDA C=O stretching mode [28–33]. On the other hand, it was unable to evaluate the hydrogen bonding between MgPc and MTPDA due to the Raman bands multiple composition, which affect the peak intensity and position.
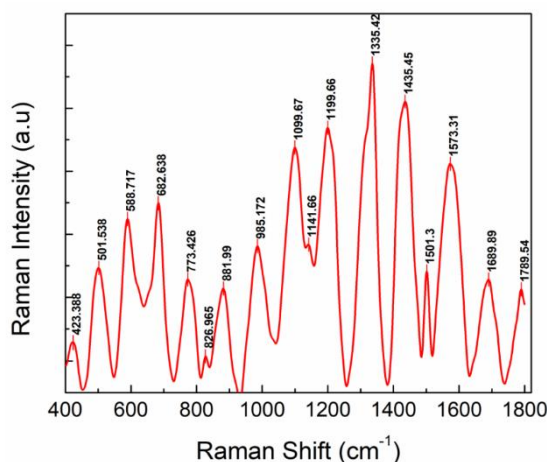
Figure 2. Raman spectrum of MgPc-MTPDA.

IR-spectrum of the MgPc-MTPDA is shown in Figure 3 and Table 1 summarized the vibration modes and their respective wavenumbers for molecule under study. The band responsible for stretch vibration in-plane pyrrole in the MgPc ring is observed at around 1332 cm^{-1} and the bands located at approximately 1291, 1165, 1118, and 752 cm^{-1} result from the interaction of carbon with hydrogen atoms [22]. In addition, the bands observed around 1606 and 1483 cm^{-1} results from a C=C stretching mode [34–36]. For MTPDA, the value around 3060 cm^{-1} correspond to the vibration of the O-H bond of the carboxylic acid C(O)O-H and it is possible to observe the band corresponding to the carbonyls of the two carboxylic acids at 1699 cm^{-1} (C=O) [17,25]. Due to the presence of the O-H vibration of the dienedioic acid, it is not possible to evaluate the presence of hydrogen bonds between the MgPc and the MTPDA. Moreover, the crystalline structure of the MgPc is another variant that can be monitored by IR spectroscopy. MPcs are known to have different polymorphs forms which are identified by the IR absorption technique [35,37–40]. It has been reported that the α-form of MgPc is characterized by a band around 720 cm^{-1}, while the β-form is characterized by a band around 778 cm^{-1} [35,37–40]. In the IR spectrum of Figure 3, it is important to notice that the signals related to the two crystalline structures are observed. Additionally, MgPc-MTPDA thin film was also evaluated by IR spectroscopy and the results are shown in Table 1. The signals agree with those reported in the literature, and with those obtained for the crystals. The above indicates a MgPc-MTPDA thermal stability and its possibility of being used as an integral part of optoelectronic devices.
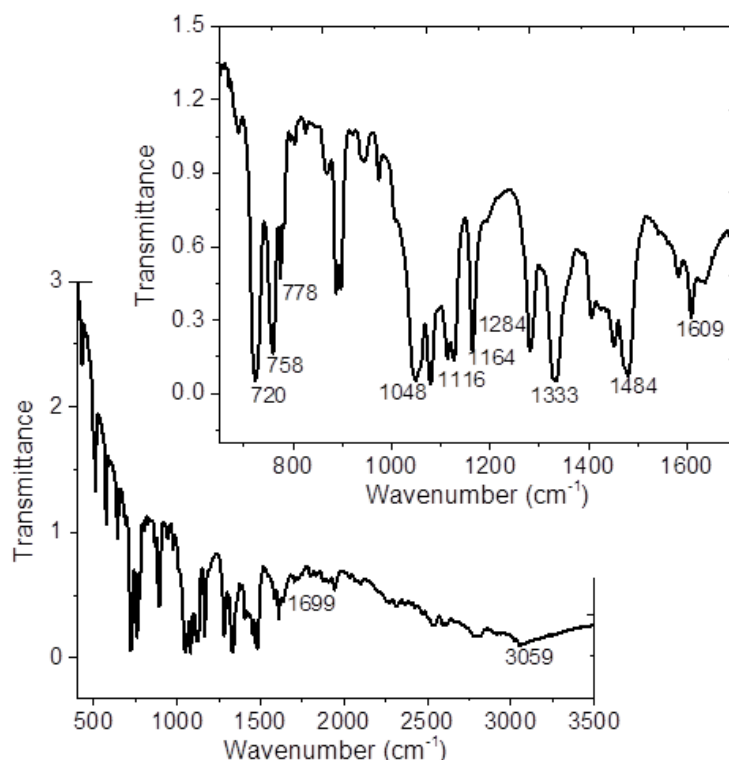
Figure 3. IR spectrum of MgPc-MTPDA.

Table 1. FT-IR spectral assignments of MgPc-MTPDA. [a] Wavenumbers (cm^{-1}) of infrared bands of References [20,32–39] for MgPc; [b] Wavenumbers (cm^{-1}) of infrared bands of References [15,23] for MTPDA.

| Assignments	MgPc and MTPDA [a,b] (cm^{-1})	MgPc-MTPDA (cm^{-1})	MgPc-MTPDA Film (cm^{-1})
In-plane pyrrole stretch	1332	1333	1330
In-plane C-H bend	1291, 1118	1284, 1116	1283, 1116
C-H bend	1165	1164	1165
In-plane C-H deformation	752	758	756
C=C benzene stretch of MgPc	1606, 1483	1609, 1484	1605, 1482
α-form of MgPc	726	720	725
β-form of MgPc	777	778	776
O-H stretching vibrations of MTPDA	3060	3059	3068
C-H vibrations of MTPDA	1699	1699	1692

Figure 4 shows the TEM micrographs as well as the selected area electron diffraction (SAED) pattern for the crystallized MgPc-MTPDA complex, which was prepared by peeling off the film from substrate and subsequently deposited on a lacey carbon copper grid. On the TEM images at different magnifications, it is possible to observe dark rounded clusters on the thin film about ~7 nm, 14 nm, and 20 nm. The inclusion is related to the crystalline phase of the MgPc, the selected area is marked in Figure 4b, where clusters are grouped. These results are in good agreement with those given in the crystallographic cards for the β MgPc. The MgPc β-phase is a monoclinic crystal with the following unit cell dimensions: a = 18.971 Å, b = 4.916 Å, c = 14.401 Å, α = γ = 90° and β = 119.89° [29,30].

The SAED pattern (Figure 4c) shows reflections with no preferential orientation that are related the MgPc-MTPDA crystals.
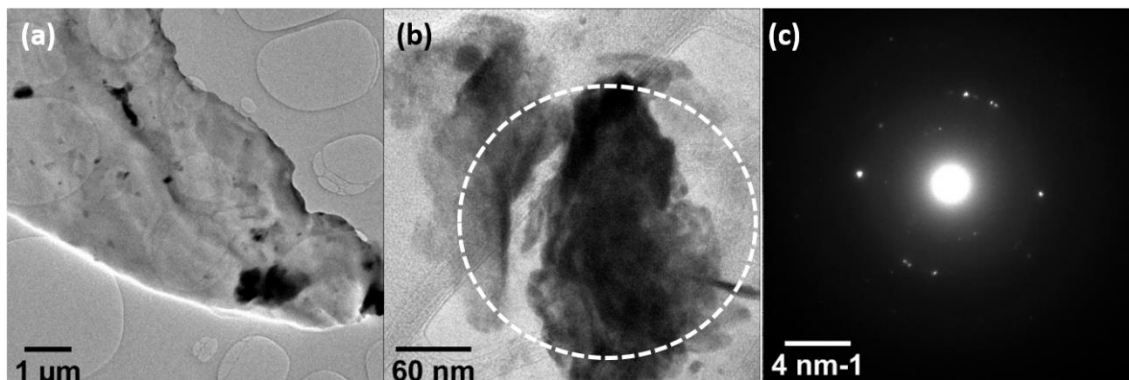
Figure 4. (**a**,**b**) TEM images of the MgPc-MTPDA with different magnifications and (**c**) is the corresponding selected area electron diffraction (SAED) pattern indicated in in the dash circle at image (**b**).

Conventional selected area electron diffraction is configured in a broad parallel illumination on the specimen. The SAED pattern of the sample is shown in Figure 5a. Low electron dose (~50 electrons/Å^2) was performed to prevent radiation damage in the sample. Under this configuration, large interplanar spacing are reflections close to the transmitted beam, which are not visible in the SAED pattern due to the low intensity produce by the lattice considering the atomic scattering factor and the neighboring with the transmitted beam, even at the low dosage. In this way, the experimental pattern shows the spots after the $\overline{2}03$ plane identified in the simulated pattern of Figure 5c. The rings showed in the Figure 5b have been compared with the simulated peaks [41], shown on Table 2. An error of 10% of the lattice parameter has been measured. The films exhibited a preferred orientation along the [001]. Moreover, indexed *hkl* planes are shown on Table 1, where the fourth ring, associated with the $\left(\overline{7}24\right)$ plane, is observed to have intense diffraction spots (Figure 5b). It is possible to observe other diffracted spots that could be related to the MTPDA doping but were no indexed.
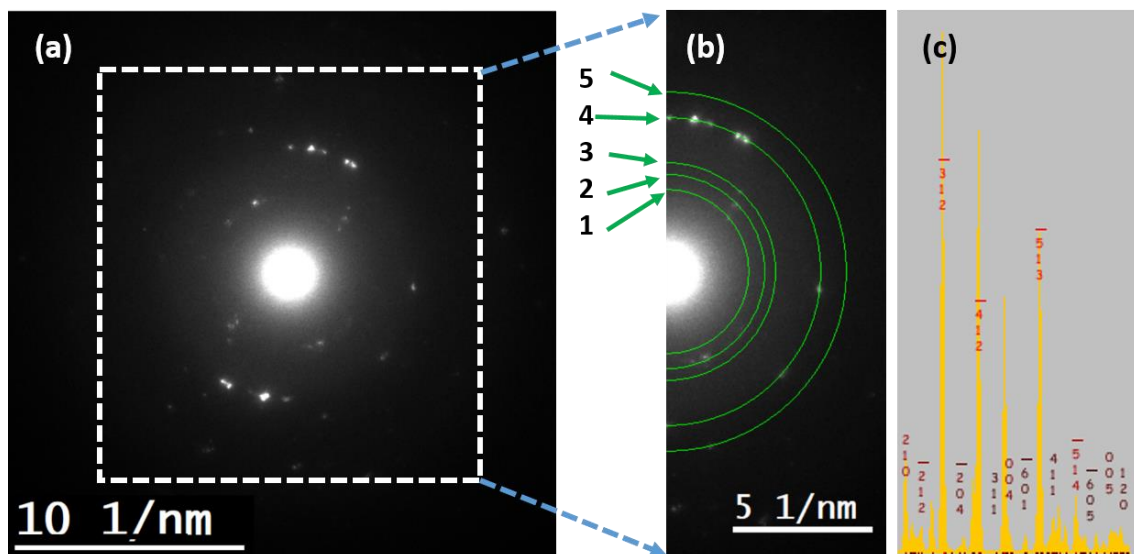

Figure 5. Analyzed (**a**) SAED pattern, (**b**) rings considered for measurements on the SAED pattern, (**c**) Simulated pattern using the java version of the electron microscopy simulation software package (JEMS).

Table 2. MgPc SAED pattern results for *d*-spacing and plane indexing compared to JEMS simulations.

| Ring	(*hkl*)	Experimental Measurement (nm)	Simulated Values (nm)
1	$(\bar{3}12)$	0.3394	0.3748
2	$(\bar{4}12)$	0.2880	0.3383
3	$(\bar{5}13)$	0.2569	0.2902
4	$(\bar{7}24)$	0.1816	0.1786
5	$(\bar{8}25)$	0.1558	0.1648

The use of vacuum thermal evaporation technique for MgPc-MTPDA produces films with high purity, quality, and uniformity. In Figure 6a the micrograph of the thin film is observed at 50×, this image presents a regular morphology with full coverage of the substrate. A uniform material layer on the film is formed, and when is analyzed at higher magnifications (Figure 6b), particles are observed because of a second stage process where nucleation and growth take place. Apparently, in the first stage, the thermal gradient between MgPc-MTPDA and the substrate caused the deposition of the doped phthalocyanine. In a second stage, the remaining MgPc-MTPDA was deposited on the first layer, in the form of small particles. When analyzing these particles at 10,000× (Figure 6c), a regular and elongated structure is observed.
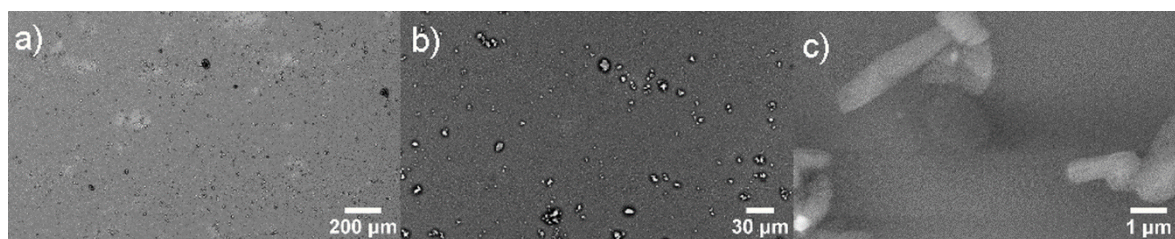
Figure 6. MgPc-MTPDA micrographs at (**a**) 50×, (**b**) 250×, and (**c**) 10,000×.

In order to verify the structure in the film, XRD was carried out and the results are shown in Figure 7a and Table 3 where the spacing between the planes (*d*) is presented. The α-phase is characterized by the peak observed at 2θ = 6.9°. This peak arises from the interlayer spacing of stacks of tilted molecules, which means that crystals are oriented with the MgPc molecular planes perpendicular to the substrate [14,42]. The peaks observed at 2θ = 24.8° and 26.9° corresponds to the β-phase [14,42,43]. The XRD patterns obtained in the film indicate a polycrystalline structure and a mixture of α- and β-phases. These results were compared with those calculated for MgPc and are shown in Figure 7b and Table 3. Moreover, similar values are observed between the theoretical and experimental diffraction patterns. It is observed a shift on the diffraction peaks 2θ, which also is a consequence of a change on planar *d*-spacing. The variations of the planar distances are as large as 0.32 Å and as small as it is equal to the theorical value. The previous observation has two contributions, the first, is related to the complex doping, indicating that the MTPDA doping process had taken place among all directions. Moreover, the MgPc-MTPDA concentration on each of the crystals, which affects the crystalline grain size, have a slight effect on the observed peak shift. Nevertheless, the existence of an equal value between experimental and theorical of the planar distance for 2θ = 25.9° (3.44 Å) indicates that there is no effect by the MTPDA doping on this direction and it is similar to the HRTEM observation for an analogous *d*-spacing. Moreover, in Table 3 the full width at half maximum (FWHM) and grain sizes for each 2θ peak are shown. The grain size is obtained from the X-ray peaks using the Scherrer formula from the FWHM of the peak: $L = K\lambda/\beta cos\theta$, where K = 0.9, λ = 1.54059 Å, β the FWHM in radians and θ the diffraction angle. It is observed that the grain size varies between 7.5 and 19.54 nm and with a 14.38 nm average size on the observed diffraction pattern. Most of

the 2θ peaks are over the average grain size. Moreover, the observed results indicate that the TEM MgPc-MTPDA clusters are formed by nanocrystalline coalescence with grains presenting different directions as observed.
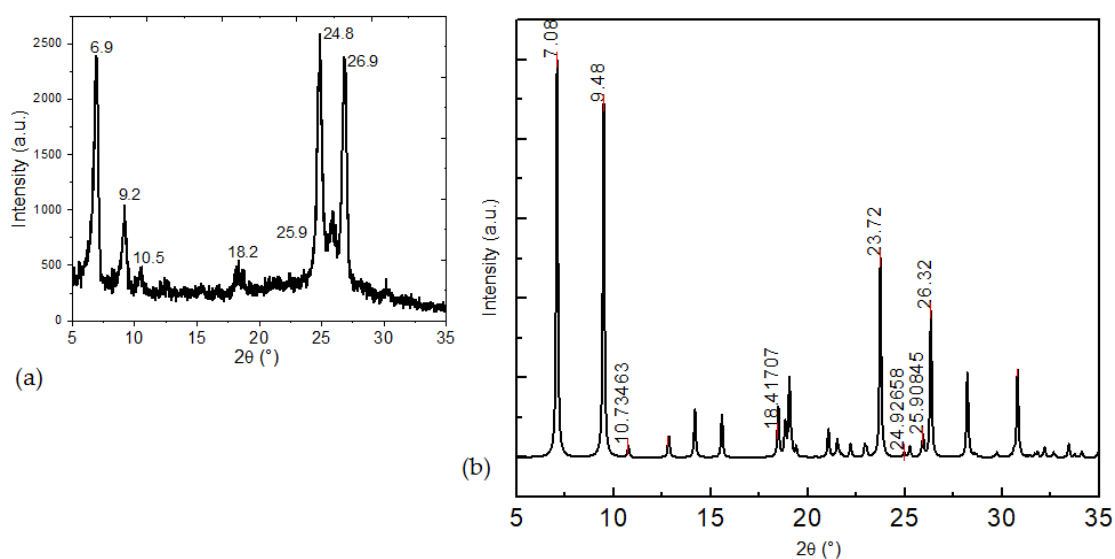

Figure 7. X-ray diffraction pattern (**a**) experimental for MgPc-MTPDA film and (**b**) calculated for MgPc.

Table 3. Spacing between the planes in MgPc-MTPDA film.

2θ (°)	6.9	9.2	10.5	18.2	24.8	25.9	26.9
d_{exp} (Å)	12.80	9.60	8.41	4.87	3.59	3.44	3.31
d_{theo} (Å)	12.48	9.32	8.24	4.81	3.57	3.44	3.38
FWHM (°)	0.4726	0.4993	0.4985	1.0723	0.5059	0.9313	0.4180
Grain size (nm)	16.84	15.96	16.00	7.50	16.08	8.75	19.54

UV–Vis spectroscopy allows to analyze the important electronic transitions in thin films. Figure 8 shows the spectra for MgPc-MTPDA film in the wavelength range 200–1000 nm, the changes of slope in the curve indicate that more than one energetic transition occurs between the energy bands of film. The spectrum shows a transparent region with a maximum at 493 nm, indicating the onset of fundamental absorption [44]. Additionally, the spectrum shows the presence of the *B*-band in the near UV region, and the *Q*-band on the red side of the spectrum. These bands are related to the molecular orbitals of the aromatic system with 18π-electrons and to the overlapping orbital on the central magnesium [22,45]. For MgPc-MTPDA, different signals can be observed: a high-energy signal, around 634 nm, and a second one, a low energy, around 691 nm. Such two signals correspond to the Q-band transition of the MgPc, assigned to the π-π* electronic transitions, due to the excitation of the electrons for the double bonds (C=C) of the aromatic rings in the isondolic units [22,45]. The broadening of the bands can be associated with the aggregation of molecules in the thin film [22,45]. Although, from the spectra, it can be observed that the MgPc-MTPDA have the *B*-band in 337 nm [22,35,45]. The electronic *n*-π* transition corresponds to a *B*-band which gives the fundamental absorption edge, the *B*-band it is due to $a_{2u}(\pi) \rightarrow e_g(\pi^*)$ together with $b_{2u}(\pi) \rightarrow e_g(\pi^*)$ transitions [22,46,47]. The signals at 261 and 294 nm are due to the presence of the dienedioic acid MTPDA. Additionally, the doublet at 691 and 634 nm, correspond to the α and β structures of phthalocyanine and also are related to the formation of singlet excitons [44,48,49].
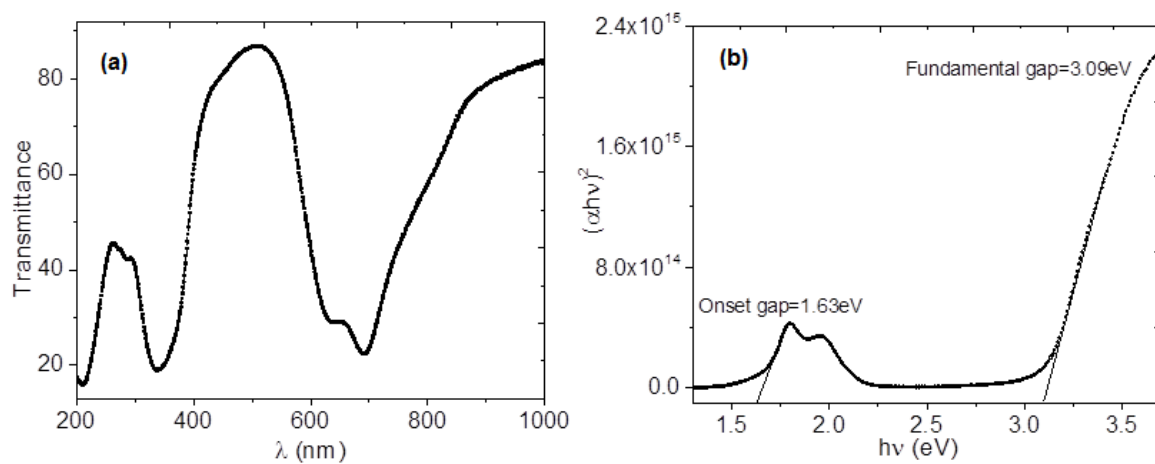
Figure 8. (**a**) The spectral distribution of transmittance and (**b**) the relation between $(\alpha h\nu)^2$ and photon energy ($h\nu$) for the MgPc-MTPDA film.

The absorption coefficient (α) was calculated from the transmission data (T) using the following equation:

$$\alpha = \frac{2.3026(1/T)}{t}, \tag{1}$$

were *t* is the thickness of the film and the energy band gap of the film was estimated using the Tauc's [50] relation given by:

$$(\alpha h\nu) = A(E_g - h\nu)^n, \tag{2}$$

were $h\nu$ is the photon energy and E_g is the optical band gap. The value of *n* characterizes the optical absorption process, which theoretically is equal to $\frac{1}{2}$, 3/2, 2, and 3 depending on the transitions, such as direct allowed, direct forbidden, indirect allowed and indirect forbidden transitions, respectively [51,52]. In the present study, the linear dependence of $(\alpha h\nu)^2$ on $h\nu$ is plotted in Figure 8b and E_g value was estimated in the linear region of the plot, to zero absorption intersection $((\alpha h\nu)^2 = 0)$, that is the characteristic behavior of direct allowed transition for crystalline films [51–53]. The exponential behavior of the graph tail indicates the presence of localized states suggesting that the film has a direct gap transition [53]. The plot in Figure 8b indicates two regions, one with higher energy called the fundamental gap at 3.09 eV and the other with a lower energy gap called the onset gap at 1.63 eV [52,53]. The reported fundamental gap for the MgPc film is 3.13 eV, while the onset gap is 1.66 eV [54], that agree with the obtained results. Apparently, the presence of dienedioic acid MTPDA has no influence on the transport of charge into the film. However, it is necessary a further study of the thin film electrical behavior by temperature variation, to determine the MgPc-MTPDA semiconductor properties.

Considering the thermal decomposition temperatures, the electrical conductivities of the MgPc-MTPDA film were measured in the 300–433 K temperature range. The obtained conductivities were around $10–10^2$ S/cm. These σ values are very similar and lie within the semiconductor region (10^{-6} to 10^2 S/cm) [48,55]. Nevertheless, comparing to previously reported undoped MgPc values, which lay between 10^{-4} and 10 S/cm [56], the conductivity of the film is increased by the incorporation of the MTPDA as dopant. Nevertheless, the previous results take in to account a uniform surface among the conduction channel length, whereas its non-uniformity could affect the conductivity results and further analysis. By analyzing the ln $\sigma = f(1000/T)$ graphs, useful electrical information regarding the conduction processes occurring in the investigated films can be obtained. The conductivity has the general form,

$$\sigma = \sigma_0 \exp\left(-\frac{E_a}{kT}\right), \tag{3}$$

where *Ea* is the thermal activation energy of the electrical conductivity, σ_0 is the pre-exponential factor depending on the material nature, and *k* is Boltzmann's constant (1.38×10^{-23} J/K). As observed on

Figure 9, a plot of *ln(σ)* versus *1000/T* yields on data points that were linear-fitted with a straight line whose slope can be used to determine the thermal activation energies of the thin films [57]. The selected temperature interval comprises an intrinsic region and extrinsic region, where impurity scattering take place. The charge conduction mechanism is interpreted as free band type and hopping, depending on the temperature region. First, it is observed that the conductivity increases with the temperature, thus the number of carriers and the mobility is increased. Finally, an activation energy of 0.21 eV was calculated for the MgPc-MTPDA and compared to intrinsic MgPc, which is in a range between 0.22 to 0.43 eV depending on the deposition conditions [54]. The latter indicates that the thermal activation energy *Ea* is decreased as the MTPDA is incorporated. Due to its capability of receiving electrons, an inferred reduction of the energy between the conduction band and the donor level of the MgPc take place. Considering the previous observation, the intrinsic high temperature region could also lead to the same effect by incorporating the dienedioic acid in the MgPc. Although, the crystallization of the film yield on a decrease of the activation energy by increasing the grain sizes. Thus, the defect density from the as-deposited samples is decreased while annealing during the crystallization process. Hence, the observed results indicate the presence of carrier trapping sites, mainly generated by the incorporated MTPDA, that dominate the steady state carriers transport properties of the organic semiconductor by the carriers hopping along with electrons, resulting from carriers escape from the trap states. Moreover, Figure 9 indicates that there are no evident marked trap levels within the material band gap. Even though, there is a distribution of trap levels, the number of levels might be affected by the MTPDA incorporation. Moreover, doping could tailor the optoelectronic properties of the material. Thus, MTPDA doped polymorphic crystalline MgPc has appropriate optoelectronic properties as an organic semiconductor to be applied on electronic devices or as active film on optoelectronic devices.
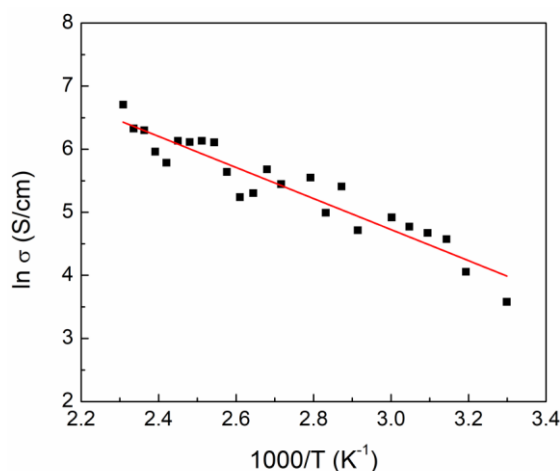

Figure 9. Arrhenius plot of the ln(σ) vs. 1000/T for the MgPc-MTPDA film.

4. Conclusions

Crystals of magnesium phthalocyanine doped with 1-(4-methoxyphenyl)-2,2,6,6-tetramethyl-5-phenylhepta-3,4-dienedioic acid were deposited. Structural and optoelectronic characterization has been conducted to understand its semiconductor properties. Raman and IR results indicate the presence of the MgPc and the MTPDA, evidenced by the characteristic vibration modes and that were supported by UV–Vis. The obtained MgPc-MTPDA polycrystalline films are constituted by a mixture of α and β phases with crystalline sizes of ~7 nm, 14 nm, and 20 nm average sizes, where grouped clusters are also observed, supported by SAED and XRD. An error of 10% of the SAED lattice parameter has been measured compared to simulated parameters. XRD evidenced that the α phase crystals are oriented with the MgPc molecular planes perpendicular to the substrate. Planes have a preferred orientation and along the [001] and MTPDA doping does not have an important effect on the distances between ring planes indicating that the molecule is among the same plane direction of the MgPc within the

complex. A uniform material layer with particles is observed as a result of a two-stage process of nucleation and growth. The UV–Vis spectrum shows a transparent region with a minimum at 483 nm, a *B*-band in 337 nm, a *Q*-band transition with a high-energy peak, around 639 nm, and a low energy peak, around 691 nm. A fundamental gap at 3.09 eV and onset gap of 1.63 eV were obtained and are similar to the undoped MgPc. Thermal conductivity measurements for the MgPc-MTPDA were done and the obtained conductivities were around 10–10^2 S/cm and activation energy of 0.21 eV.

Author Contributions: Conceptualization, L.H. and M.E.S.-V.; Data curation, L.H. and C.Á.-T.; Formal analysis, L.H., M.E.S.-V. and A.P.; Investigation, L.H., M.E.S.-V., R.S.-R., C.Á.-T., J.L.R.-R. and A.P.; Methodology, M.E.S.-V., R.S.-R. and A.P.; Writing—original draft, L.H. and M.E.S.-V.; Writing—review and editing, M.E.S.-V., and A.P. All authors have read and agreed to the published version of the manuscript.

Conflicts of Interest: The authors declare no conflict of interest.

References

1. Sworakowski, J.; Ulański, J. Electrical properties of organic materials. *Annu. Rep. Prog. Chem. Sect. C Phys. Chem.* **2003**, *99*, 87–125. [CrossRef]
2. Wang, L.; Nan, G.; Yang, X.; Peng, Q.; Li, Q.; Shuai, Z. Computational methods for design of organic materials with high charge mobility. *Chem. Soc. Rev.* **2010**, *39*, 423–434. [CrossRef] [PubMed]
3. Sun, S.S.; Dalton, L.R. *Introduction to Organic Electronic and Optoelectronic Materials and Devices*; CRC Press: London, UK, 2005.
4. Plows, F.L.; Jones, A.C. Laser-Desorption Supersonic Jet Spectroscopy of Phthalocyanines. *J. Mol. Spectrosc.* **1999**, *194*, 163–170. [CrossRef] [PubMed]
5. Salcedo, R.; Pérez, L.; Sánchez-Vergara, M.E. Spectroscopic studies and density functional theory investigations of a cobalt phthalocyanine derivative. *J. Mol. Struct.* **2015**, *1084*, 165–171. [CrossRef]
6. Özçesmeci, M.; Bülent, Ö.; Sürgün, S.; Hamuryudan, E. Tetracationic fluorinated zinc(ii)phthalocyanine: Synthesis, characterization and DNA-binding properties. *Dyes Pigm.* **2012**, *96*, 52–58. [CrossRef]
7. Sánchez-Vergara, M.E.; Rivera, M. Investigation of optical properties of annealed aluminum phthalocyanine derivatives thin films. *J. Phys. Chem. Solids* **2014**, *75*, 599–605. [CrossRef]
8. Rodríguez, A.; Sánchez-Hernández, C.M.; Fleitman-Levin, I.; Arenas-Alatorre, J.; Alonso-Huitrón, J.C.; Sánchez-Vergara, M.E. Optical Absorption and Visible Photoluminescence from Thin Films of Silicon Phthalocyanine Derivatives. *Materials* **2014**, *7*, 6585–6603. [CrossRef]
9. Lim, B.; Margulis, G.Y.; Yum, J.; Unger, E.L.; Hardin, B.E.; Grätzel, M.; McGehee, M.D.; Sellinger, A. Silicon-Naphthalo/Phthalocyanine-Hybrid Sensitizer for Efficient Red Response in Dye-Sensitized Solar Cells. *Org. Lett.* **2013**, *15*, 784–787. [CrossRef]
10. Sánchez-Vergara, M.E.; Hamui, L.; González Habib, S. New Approaches in Flexible Organic Field-Effect Transistors (FETs) Using InClPc. *Materials* **2019**, *12*, 1712. [CrossRef]
11. Eken, S.; Temel, G.; Karaca, D.; Arsu, N.; Sener, M.K. Type II photoinitiator substituted zinc phthalocyanine: Synthesis, photophysical and photopolymerization studies. *J. Lumin.* **2013**, *136*, 389–394. [CrossRef]
12. Nieto, E.; Fernández, J.F.; Duran, P.; Moure, C. Boletín de la Sociedad Española de Cerámica y Vidrio. *Películas Delgadas Fabr. Apl.* **1994**, *33*, 245–258.
13. Rivera, M.; Reyes, B.; Sánchez-Vergara, M.E.; Mendoza-Huiza, L.H. Conductive Behavior and Morphology of Axially Modified Gallium Phthalocyanine Thin Films onto Indium Tin Oxide Substrates. *Mater. Chem. Phys.* **2016**, *6*, 211–219. [CrossRef]
14. Della Pirriera, M.; Puigdollers, J.; Voz, C.; Stella, M.; Bertomeu, J.; Alcubilla, R. Optoelectronic properties of CuPc thin films deposited at different substrate temperatures. *J. Phys. D Appl. Phys.* **2009**, *42*. [CrossRef]
15. Basova, T.V.; Kiselev, V.G.; Plyashkevich, V.A.; Cheblakov, P.B.; Latteyer, F.; Peisert, H.; Chassè, T. Orientation and morphology of chloroaluminum phthalocyanine films grown by vapor deposition: Electrical field-induced molecular alignment. *Chem. Phys.* **2011**, *380*, 40–47. [CrossRef]

16. El-Nahass, M.M.; Ammar, A.H.; Farag, A.A.M.; Atta, A.A.; El-Zaidia, E.F.M. Effect of heat treatment on morphological, structural and optical properties of CoMTPP thin films. *Solid State Sci.* **2011**, *13*, 596–600. [CrossRef]

17. Sánchez-Vergara, M.E.; Leyva-Esqueda, E.A.; Álvarez, C.; López Reyes, M.; Miralrio, A.; Salcedo, R. Influence of TCNQ acceptor on optical and electrical properties of tetrasubstituted allenes films fabricated by vacuum termal evaporation. *J. Mater. Sci. Mater. Electron.* **2016**, *27*, 9900–9910. [CrossRef]

18. Gould, R.D. Structure and electrical conduction properties of phtalocyanine thin films. *Coord. Chem. Rev.* **1996**, *156*, 237–274. [CrossRef]

19. Bovill, A.J.; McConnell, A.A.; Nimmo, J.A.; Smith, W.E. Resonance Raman Spectra of α-Copper Phthalocyanine. *J. Phys. Chem.* **1986**, *90*, 569–575. [CrossRef]

20. Liu, Z.T.; Kwok, H.S.; Djurišić, A.B. The optical functions of metal phthalocyanines. *J. Phys. D Appl. Phys.* **2004**, *37*, 678–688. [CrossRef]

21. Brozek-Płuska, B.; Szymczyk, I.; Abramczyk, H. Raman spectroscopy of phthalocyanines and their sulfonated derivatives. *J. Mol. Struct.* **2005**, *744–747*, 481–485. [CrossRef]

22. Hamui, L.; Sánchez-Vergara, M.E.; Sánchez-Ruiz, R.; Ruanova-Ferreiro, D.; Ballinas, R.; Álvarez-Toledano, C. New Development of Membrane Based Optoelectronic Devices. *Polymers* **2018**, *10*, 16. [CrossRef]

23. Ma, S. Some Typical Advances in the Synthetic Applications of Allenes. *Chem. Rev.* **2005**, *105*, 2829–2871. [CrossRef] [PubMed]

24. Rand, B.P.; Cheyns, D.; Vasseur, K.; Giebink, N.C.; Mothy, S.; Yi, Y.; Coropceanu, V.; Beljonne, D.; Cornil, J.; Brédas, J.L.; et al. The impact of molecular orientation on the photovoltaic properties of a phthalocyanine/fullerene heterojunction. *Adv. Funct. Mater.* **2012**, *22*, 2987–2995. [CrossRef]

25. Alcarazo, M. On the metallic nature of carbon in allenes and heterocumulenes. *Dalton. Trans.* **2011**, *40*, 1839–1845. [CrossRef]

26. López-Reyes, M.E.; López-Cortés, J.G.; Ortega-Alfaro, M.C.; Toscano, R.A.; Álvarez-Toledano, C. First direct synthesis of 3-hydroxy-pent-4-ynoic acids. Application to the synthesis of pyran-2-ones. *Tetrahedron* **2013**, *69*, 7365–7372. [CrossRef]

27. Stadelmann P: JEMS. Available online: https://www.epfl.ch/research/facilities/cime/research/research-jems/ (accessed on 15 April 2020).

28. Defeyt, C.; Vandenabeele, P.; Gilbert, B.; Van Pevenage, J.; Cloots, R.; Strivay, D. Contribution to the identification of α-, β- and ε-copper phthalocyanine blue pigments in modern artists' paints by X-ray powder diffraction, attenuated total reflectance micro-fourier transform infrared spectroscopy and micro-Raman spectroscopy. *J. Raman Spectrosc.* **2012**, *43*, 1772–1780. [CrossRef]

29. Tóbik, J.; Tosatti, E. Raman tensor calculation for magnesium phthalocyanine. *Surf. Sci.* **2006**, *600*, 3995–3998. [CrossRef]

30. Loutfy, R.O.; Hor, A.M.; Dipaola-Baranyi, G.; Hsiao, C.K. Electrophotographic photoreceptors incorporation aggregated phthalocyanines. *J. Imaging Sci.* **1985**, *29*, 116. [CrossRef]

31. Kavelin, V.; Fesenko, O.; Dubyna, H.; Vidal, C.; Klar, T.A.; Hrelescu, C.; Dolgov, L. Raman and Luminescent Spectra of Sulfonated Zn Phthalocyanine Enhanced by Gold Nanoparticles. *Nanoscale Res. Lett.* **2017**, *12*, 197–204. [CrossRef]

32. Schäfer, P.; Himcinschi, C.; Chis, V.; Zahn, D.R.T. In situ Raman growth monitoring of indium/copper phthalocyanine interfaces. *Phys. Status Solidi* **2010**, *7*, 232–235. [CrossRef]

33. Jennings, C.; Aroca, R.; Hor, A.M.; Loutfy, R.O. Raman spectra of solid films 3—Mg, Cu and Zn phthalocyanine complexes. *J. Raman Spectrosc.* **1984**, *15*, 34–37. [CrossRef]

34. Touka, N.; Benelmadjat, H.; Boudine, B.; Halimi, O.; Sebais, M. Copper phthalocyanine nanocrystals embedded into polymer host: Preparation and structural characterization. *J. Assoc. Arab Univ. Basic Appl. Sci.* **2013**, *13*, 52–56. [CrossRef]

35. El-Nahass, M.M.; Abd-El-Rahman, K.F.; Al-Ghamdi, A.A.; Asiri, A.M. Optical properties of thermally evaporated tin-phthalocyanine dichloride thin films, $SnPcCl_2$. *Phys. B Condens. Matter* **2014**, *344*, 398–406. [CrossRef]

36. Hart, M.M. Cationic Exchange Reactions Involving Dilithium Phthalocyanine. Master's Thesis, Wright State University, Dayton, OH, USA, 2009.

37. El-Nahass, M.M.; Farag, A.M.; Abd-El-Rahman, K.F.; Darwish, A.A.A. Dispersion studies and electronic transitions in nickel phthalocyanine thin films. *Opt. Laser Technol.* **2005**, *37*, 513–523. [CrossRef]

38. Karan, S.; Basak, D.; Mallik, B. Persistence in photoconductivity and optical property of nanostructured copper (II) phthalocyanine thin films. *Curr. Appl. Phys.* **2010**, *10*, 1117–1122. [CrossRef]

39. Wang, J.B.; Li, W.L.; Chu, B.; Lee, C.S.; Su, Z.S.; Zhang, G.; Wu, S.H.; Yan, F. High speed responsive near infrared photodetector focusing on 808 nm radiation using hexadeca-fluoro–copper–phthalocyanine as the acceptor. *Org. Electron.* **2011**, *12*, 34–38. [CrossRef]

40. Neghabi, M.; Zadsar, M.; Ghorashi, S.M.B. Investigation of structural and optoelectronic properties of annealed nickel phthalocyanine thin films. *Mater. Sci. Semicond. Process.* **2014**, *17*, 13–20. [CrossRef]

41. Mizuguchi, J. Crystal structure of magnesium phthalocyanine, C~32~H~16~N~8~Mg. *Z. Kristallogr. New Cryst. Struct.* **2001**, *216*, 377–378.

42. Akamatsu, K.; Deki, S. Characterization and optical properties of gold nanoparticles dispersed in nylon 11 thin films. *J. Mater. Chem.* **1997**, *7*, 1773–1777. [CrossRef]

43. Vasseur, K.; Rand, B.P.; Cheyns, D.; Froyen, L.; Heremans, P. Structural Evolution of Evaporated Lead Phthalocyanine Thin Films for Near-Infrared Sensitive Solar Cells. *Chem. Mater.* **2011**, *23*, 886–895. [CrossRef]

44. Azim-Araghi, M.E.; Krier, A. Optical characterization of chloroaluminium phthalocyanine (ClAlPc) thin films. *Pure Appl. Opt.* **1997**, *6*, 443–453. [CrossRef]

45. Socol, M.; Preda, N.; Rasoga, O.; Breazu, C.; Stavarache, I.; Stanculescu, F.; Socol, G.; Gherendi, F.; Grumezescu, V.; Popescu-Pelin, G.; et al. Flexible heterostructures based on metal phthalocyanines thin films obtained by MAPLE. *Appl. Surf. Sci.* **2016**, *374*, 403–410. [CrossRef]

46. Regimol, C.C.; Menon, C.S. Effect of annealing and Gamma irradiation on tin phthalocyanine thin films. *Mater. Sci. Poland* **2007**, *25*, 649–655.

47. Novotny, M.; Bulir, J.; Bensalah-Ledoux, A.; Guy, S.; Fitl, P.; Vrnata, M.; Lancok, J.; Moine, B. Optical properties of zinc phthalocyanine thin films prepared by pulsed laser deposition. *Appl. Phys. A* **2014**, *117*, 377–381. [CrossRef]

48. Laurs, H.; Heiland, G. Electrical and optical properties of phthalocyanine films. *Thin Solid Films* **1987**, *149*, 129–142. [CrossRef]

49. Simonyan, M.; Kafadaryan, E.A.; Murijanyan, M.C.; Petresion, A.K.; Sharoyan, E.G. ESR, optical absorption and reflection spectra of monoclinic and triclinic modifications of lead phthalocyanine. *Phys. Stat. Sol.* **1987**, *101*, 143–149. [CrossRef]

50. Tauc, J. Optical properties and electronic structure of amorphous Ge and Si. *Mater. Res. Bull.* **1968**, *3*, 37–46. [CrossRef]

51. Mohana, J.; Ahila, G.; Bharathi, M.D.; Anbalagan, G. Growth, spectral, optical, thermal, and mechanical behaviour of an organic single crystal: Quinolinium 2-carboxy 6-nitrophthalate monohydrate. *J. Cryst. Growth* **2016**, *450*, 181–189. [CrossRef]

52. El-Nahass, M.M.; Sallam, M.M.; Ali, H.A.M. Optical properties of thermally evaporated metal-free phthalocyaninde (H_2Pc) thin films. *Int. J. Mod. Phys. B* **2005**, *19*, 4057–4071. [CrossRef]

53. Painuly, D.; Masram, D.T.; Rabanal, M.E.; Nagpure, L.M. The effect of ethanol on structural, morphological and optical properties of Li(I) 8–hydroxyquinoline phosphor. *J. Lumin.* **2017**, *192*, 1180–1190. [CrossRef]

54. Seoudi, R.; El-Bahy, G.S.; El Sayed, Z.A. Ultraviolet and visible spectroscopic studies of phthalocyanine and its complexes thin films. *Opt. Mater.* **2006**, *29*, 304–312. [CrossRef]

55. Kiani, M.S.; Mitchell, G.R. Structure property relationships in electrically conducting copolymers formed from pyrrole and *N*-methyl pyrrole. *Synth. Met.* **1992**, *46*, 293–306. [CrossRef]

56. Gopinathan, T.G.; Menon, C.S. Studies on the electrical and optical properties of magnesium phthalocyanine thin films. *E J. Chem.* **2004**, *1*, 231–236. [CrossRef]

57. Sarkar, S.; Aydogdu, A.; Dagdelen, F.; Bhaumik, B.B.; Dey, K. X-ray diffraction studies, thermal, electrical and optical properties of oxovanadium(IV) complexes with quadridentate schiff bases. *Mater. Chem. Phys.* **2004**, *88*, 357–363. [CrossRef]